

Reduced kinetic modelling of shattered pellet injection in ASDEX Upgrade

P. Haldestam¹†, P. Heinrich¹, G. Papp¹, M. Hoppe², M. Hoelzl¹,
I. Pusztai³, O. Vallhagen³, R. Fischer¹, F. Jenko¹, the ASDEX
Upgrade Team^a, and the EUROfusion Tokamak Exploitation Team^b

¹Max Planck Institute for Plasma Physics, Garching, Germany

²Department of Electrical Engineering, Royal Institute of Technology, Stockholm, Sweden

³Department of Physics, Chalmers University of Technology, Göteborg, Sweden

^aSee the author list of H. Zohm *et al.* (2024) Nucl. Fusion

^bSee the author list of E. Joffrin *et al.* (2024) Nucl. Fusion

(Received xx; revised xx; accepted xx)

Plasma-terminating disruptions represent a critical outstanding issue for reactor-relevant tokamaks. ITER will use shattered pellet injection (SPI) as its disruption mitigation system to reduce heat loads, vessel forces, and to suppress the formation of runaway electrons. In this paper we demonstrate that reduced kinetic modelling of SPI is capable of capturing the major experimental trends in ASDEX Upgrade SPI experiments, such as dependence of the radiated energy fraction on neon content, or the current quench dynamics. Simulations are also consistent with the experimental observation of no runaway electron generation with neon and mixed deuterium-neon pellet composition. We also show that statistical variations in the fragmentation process only have a notable impact on disruption dynamics at intermediate neon doping, as was observed in experiments.

Key words: tokamak disruptions, shattered pellet injection, plasma dynamics

1. Introduction

One of the main issues threatening the success of future reactor-scale tokamaks is disruptions. It is the sudden loss of confinement, where the plasma rapidly ejects a large portion of its energy content onto the first wall, which exposes the device to excessive mechanical stresses, heat loads, and can lead to the formation of a runaway electron beam (Hender *et al.* 2007; Breizman *et al.* 2019). Unmitigated disruptions could potentially cause severe damage to the device, and modelling such events is thus crucial to assess the effectiveness of various mitigation techniques and to optimise termination scenarios.

Shattered pellet injection (SPI) employs hydrogen with minority neon admixture, frozen into cryogenic pellets, which are launched into the vessel at speeds of several hundred meters per second. Upon entry, the singular pellet is broken into smaller pieces by a shattering unit to increase pellet material ablation and assimilation into the plasma. The exact pellet composition, penetration velocity, and the size distribution of pellet fragments has major impact on the disruption mitigation efficiency. Modelling is crucial to understand the complex physics and to optimise the termination scenarios.

† Email address for correspondence: peter.haldestam@ipp.mpg.de

The ITER baseline disruption mitigation system will be based on SPI due to its ability to promptly inject material into the plasma to thermally radiate its stored energy, reduce electromagnetic loads on the surrounding conducting structures, and to inhibit the generation of runaway electrons (Hollmann *et al.* 2014; Lehnen *et al.* 2015; Jachmich *et al.* 2021; Vallhagen *et al.* 2024a). As the mitigation of the various disruption consequences, however, poses conflicting criteria, finding an optimised scheme is not straightforward requiring experimental and theoretical input. In support of its development, a highly flexible SPI system was installed at the ASDEX Upgrade (AUG) tokamak for the 2021/2022 SPI experimental campaign to investigate the impact of different fragment size and velocity distributions on the disruption dynamics (see Dibon *et al.* 2023; Heinrich *et al.* 2024a).

High-fidelity magnetohydrodynamic (MHD) simulations are routinely applied to disruption modelling, e.g. with JOREK (Hoelzl *et al.* 2021; Nardon *et al.* 2020; Hu *et al.* 2021; Tang *et al.* 2024) or NIMROD (Sovinec *et al.* 2004; Kim *et al.* 2019), representing the high physics fidelity – high numerical cost end of the spectrum. To carry out large parameter scans, aid design decisions, and help focus expensive simulations where most needed, reduced models are also employed. In this paper, the one-dimensional fluid model of the DREAM code (Disruption Runaway Electron Analysis Model, by Hoppe *et al.* (2021)) is used.

This code has been used for simulations of ITER (Pusztai *et al.* 2022; Lier *et al.* 2023; Ekmark *et al.* 2024; Vallhagen *et al.* 2024a) as well as TCV (Wijkamp *et al.* 2023), JET (Järvinen *et al.* 2022), DIII-D (Izzo *et al.* 2022; Marini *et al.* 2024), STEP (Berger *et al.* 2022; Fil *et al.* 2024), and SPARC (Izzo *et al.* 2022; Tinguely *et al.* 2023). In this paper we demonstrate that DREAM can explain experimental trends of major disruption characteristics at AUG, such as the evolution of the plasma current I_p or the radiated energy fraction f_{rad} .

The plume of fragments used as input for the modelling is generated by sampling fragment size and velocity distributions that depend on various injection parameters, such as the pellet neon fraction f_{Ne} and the injection speed v_{inj} , using the Parks model (Parks 2016) as implemented by Gebhart *et al.* (2020a). Since pellet fragmentation is a statistical process, we simulate an ensemble of several realisations for each parameter set, to assess the impact that statistical variation in the fragment distribution has on the resulting disruption dynamics (sensitivity analysis).

The physics model used is detailed in sections 2.1 and 2.2, followed by a description on the fragment sampling in section 2.3. An overview of the simulation setup and the AUG SPI discharges selected for the experimental comparison is presented in section 2.4 and 2.5, respectively. A demonstrative scan in the pellet neon fraction is detailed in section 3.1, and the experimental comparison in section 3.2. The results and limitations of the model are discussed and concluded in section 4.

2. Methods

2.1. Physics model

A one-dimensional fluid model of the plasma available in the DREAM code is applied. This is a finite-volume numerical simulation framework that has been developed for tokamak disruption modelling, with a particular focus on the runaway electron dynamics. It evolves the plasma current self-consistently, along with the thermal bulk of electrons, and charge states of the relevant ionic species – all in a realistic toroidally symmetric magnetic geometry. In this section, the relevant equations and physical assumptions are described in detail.

Plasma current

The plasma current density j_{\parallel} consists of an Ohmic component j_{Ω} , and a component j_{re} carried by runaway electrons. Other non-inductively driven currents, such as the bootstrap current, are not included in this model as these are expected to vanish quickly in a disruption. The total current density is related to the poloidal magnetic flux ψ_{p} , as described by Ampère’s law

$$2\pi\mu_0 \langle \mathbf{B} \cdot \nabla\varphi \rangle \frac{j_{\parallel}}{B} = \frac{1}{V'} \frac{\partial}{\partial r} V' \left\langle \frac{|\nabla r|^2}{R^2} \right\rangle \frac{\partial\psi_{\text{p}}}{\partial r}, \quad (2.1)$$

where $\langle \cdot \rangle$ denotes flux surface average, \mathbf{B} the magnetic field, R the major radius, and V' is the spatial Jacobian ($dV = V' dr$ being the volume between two infinitesimally close flux surfaces). These depend on the particular magnetic equilibrium $\mathbf{B}(r, \theta)$ used in the simulation setup, which is treated as static in this model. Note that radial coordinate r is defined as the distance on the midplane from the magnetic axis $R = R_0$ to the corresponding flux surface on the high-field side.

The poloidal magnetic flux ψ_{p} is evolved using a modified version of Faraday’s law of induction

$$\frac{\partial\psi_{\text{p}}}{\partial t} = -2\pi \frac{\langle \mathbf{E} \cdot \mathbf{B} \rangle}{\langle \mathbf{B} \cdot \nabla\varphi \rangle} + \mu_0 \frac{\partial}{\partial\psi_{\text{t}}} \psi_{\text{t}} \Lambda \frac{\partial}{\partial\psi_{\text{t}}} \frac{j_{\parallel}}{B}. \quad (2.2)$$

This is the loop voltage, of which the first term on the right-hand side is proportional to the electric field parallel to the magnetic field driving the Ohmic component of the current according to Ohm’s law $j_{\Omega}/B = \sigma \langle \mathbf{E} \cdot \mathbf{B} \rangle / \langle B^2 \rangle$. The parallel electric conductivity is modelled as outlined in Redl *et al.* (2021). It is a neoclassical correction of the Spitzer conductivity $\sigma \propto T_e^{3/2}$ accounting for trapped particle effects at arbitrary collisionality.

The second term in equation (2.2), derived by Boozer (1986), involves a second-order derivative in the toroidal magnetic flux $\psi_{\text{t}} = (2\pi)^{-1} \int V' dr \langle \mathbf{B} \cdot \nabla\varphi \rangle$, which is used as a radial coordinate. Given the relation in equation (2.1), this term is in fact a fourth-order radial derivative, and thus describes the hyperdiffusion of ψ_{p} . Whenever Λ is greater than zero, this term acts to relax j_{\parallel}/B while conserving the helicity content of the plasma. This leads to a transient increase in I_{p} as the current density radially redistributes in what is referred to as the “ I_{p} -spike”. This emulates the effects that the break-up of magnetic field lines has on the current density, and is used to model the enhanced transport event during the thermal quench phase of a disruption with strong field stochasticisation. This is explained in more detail in section 2.2.

As boundary condition for the plasma edge flux $\psi_{\text{p}}(a)$, we couple it to an ideally conducting wall at $r = b > a$. By doubly integrating equation (2.1) over the vacuum region $a < r < b$, in which $j_{\parallel} = 0$, we can relate the plasma edge flux to that of the wall $\psi(b) = \psi(a) + M_{\text{ab}} I_{\text{p}}$, where $M_{\text{ab}} = \mu_0 R_0 \ln(b/a)$ is the edge-wall mutual flux inductance taken in the cylindrical limit $a/R \rightarrow 0$. We consider a wall that is perfectly conducting, meaning no electric field is induced in the wall and thus the wall flux remains constant in time.

In addition to the Ohmic component, the plasma current can also contain a component driven by runaway electrons. Without resolving the electron distribution in momentum space, the runaway electrons are assumed to travel at the speed of light c , and their contribution to the total plasma current density is given by $j_{\text{re}} = ec n_{\text{re}}$, with e being the elementary charge. The evolution of the runaway density n_{re} also includes diffusive transport with $D_{\text{re}} = 1 \text{ m}^2/\text{s}$, and a set of source terms accountin for the runaway electron generation mechanisms. These include Dreicer generation, which is calculated by a neural network that has been trained on kinetic simulations (Hesslow *et al.* 2019*b*; Ekmark *et al.*

2024); hot-tail generation, as calculated in section 4.2 of Svenningsson (2020); and a model for the avalanche growth rate, which accounts for partial screening effects in non-ideal plasmas (Hesslow *et al.* 2019a). A negligible generation of runaways is expected for the plasma scenarios considered in this work, but the respective terms are included for completeness as these models are readily available in DREAM and are relatively inexpensive computationally. Runaway electrons were so far not observed in ASDEX Upgrade SPI experiments with neon and deuterium-neon injections. Our simulations help explain that this is due to insufficient generation, rather than due to runaway seed losses preventing avalanche.

Ions and SPI dynamics

Ions are characterised both by a temperature T_i , and a set of densities $n_i^{(j)}$ for every species i with atomic number Z_i , and charge state $j = 0, \dots, Z_i$. The densities are evolved according to

$$\begin{aligned} \frac{\partial n_i^{(j)}}{\partial t} = & \mathcal{I}_i^{(j-1)} n_i^{(j-1)} n_e - \mathcal{I}_i^{(j)} n_i^{(j)} n_e + \mathcal{R}_i^{(j+1)} n_i^{(j+1)} n_e - \mathcal{R}_i^{(j)} n_i^{(j)} n_e \\ & + \delta_{0j} \sum_{k=1}^{N_{\text{frag}}} \mathcal{G}_k \frac{\delta(r - r_k)}{4\pi r^2 R_0} + \frac{1}{V'} \frac{\partial}{\partial r} V' \left(A_i n_i^{(j)} + D_i \frac{\partial n_i^{(j)}}{\partial r} \right). \end{aligned} \quad (2.3)$$

The first four terms describe ionisation and recombination processes, for which the coefficient $\mathcal{I}_i^{(j)}$ denotes the rate of ionisation between the two charge states $j \rightarrow j + 1$, and $\mathcal{R}_i^{(j)}$ the rate of recombination between $j \rightarrow j - 1$. These coefficients are extracted from the OpenADAS database (Summers 2004).

The fifth term describes a source into the neutral state of the injected material, as the fragments travel along their paths $r_k(t)$, $k = 1, \dots, N_{\text{frag}}$, and depositing ablated material. The rate at which a fragment decreases in diameter $d_k(t)$ is calculated as $\dot{d}_k = -2\mathcal{G}_k \mathcal{M} / (\pi d_k^2 \rho N_A)$, where \mathcal{M} is the pellet molar mass, ρ the pellet mass density, and N_A Avogadro's number. The rate of the deposition of neutrals per unit time \mathcal{G}_k is calculated using a version of the Neutral Gas Shielding (NGS) model, first derived by Parks & Turnbull (1978) and further extended upon by Parks (2017) to allow for mixed deuterium-neon pellets. The NGS model provides the scaling law $\mathcal{G}_k \propto \lambda n_e^{1/3} T_e^{5/3} d_k^{4/3}$, where λ (along with \mathcal{M} and ρ) is a function of the neon fraction of the pellet $f_{\text{Ne}} = N_{\text{Ne}} / (N_{\text{D}_2} + N_{\text{Ne}})$.

The sixth and final term in equation (2.3) describes both advective and diffusive particle transport, for which the transport coefficients A_i and D_i are active during the thermal quench (similarly to Λ). More on this in section 2.2.

For each ion species, a temperature T_i , which is assumed to be same for all charge states, is evolved via collisional heat exchange with the bulk electron population and other ion species present in the plasma, according to

$$\frac{3}{2} \frac{\partial n_i T_i}{\partial t} = \sum_{i'} Q_{ii'} + Q_{ie}, \quad (2.4)$$

with the total density $n_i = \sum_{j=0}^{Z_i} n_i^{(j)}$. Here $Q_{\alpha\beta}$ is the collisional heat exchange between Maxwellian species α and β , which is proportional to their temperature difference, as further detailed in Hoppe *et al.* (2021).

Thermal electrons

The evolution of the electron temperature T_e is modelled using an energy balance equation

$$\begin{aligned} \frac{3}{2} \frac{\partial n_e T_e}{\partial t} = & \frac{j\Omega}{B} \langle \mathbf{E} \cdot \mathbf{B} \rangle - n_e \sum_i \sum_{j=0}^{Z_i-1} L_i^{(j)} n_i^{(j)} + \mathcal{P}_{\text{ion}} \\ & + \frac{j_{\text{re}}}{B} \langle B \rangle E_c + \sum_i Q_{ei} + \frac{1}{V'} \frac{\partial}{\partial r} V' \frac{3n_e}{2} \chi_e \frac{\partial T_e}{\partial r}, \end{aligned} \quad (2.5)$$

in which the first term on the right-hand side describes Ohmic heating, and the second radiative cooling due to line radiation, recombination radiation and bremsstrahlung. Integrating this term over the plasma volume yields the total radiated power, which we will denote as P_{rad} . Typically, this energy balance is dominated by Ohmic heating and radiative cooling, both of which are nonlinear functions of the electron temperature. The rates of energy loss $L_i^{(j)}(n_e, T_e)$ for neon are retrieved from OpenADAS (Summers 2004). Deuterium is instead assumed to be opaque to Lyman radiation, which reduces the radiative losses at temperatures below 10 eV; for this the loss rates are extracted from the AMJUEL database (Reiter 2020).

The third term, \mathcal{P}_{ion} , represents the change in potential energy due to the electron-ion binding energy removed by the electron bulk during ionisation and added during recombination. With the ionisation threshold energies $\Delta W_i^{(j)}$ obtained from the NIST database (Kramida *et al.* 2020), this contribution to the energy balance is calculated by adding up the terms $\Delta W_i^{(j)}(\mathcal{R}_i^{(j)} - \mathcal{I}_i^{(j)})n_i^{(j)}n_e$ over all charge states.

Collisional heat transfer from the runaway electrons is accounted for with the fourth term, where $E_c = n_e e^3 \ln \Lambda / (4\pi \varepsilon_0^2 m_e c^2)$. The fifth term is the collisional heat transfer between electrons and ions $Q_{ei} = -Q_{ie}$, and the final term describes diffusive heat transport, with χ_e being the heat diffusivity. A baseline value of $\chi_e = 1 \text{ m}^2/\text{s}$ is used throughout.

2.2. Enhanced transport event

To emulate the effect of the magnetic field stochastisation during the thermal quench that causes the thermal energy loss, an enhanced radial transport of heat, particles and poloidal magnetic flux is applied at a time t_{relax} . As previously done in ITER studies by Vallhagen *et al.* (2024a), we take t_{relax} to be the time when the electron temperature drops below 10 eV somewhere inside of the resonant $q = 2$ surface. The choice of this particular criterion for triggering the enhanced transport event is motivated by the fact that the conductivity at 10 eV is sufficiently low to likely trigger a resistive MHD instability at the resonant $q = 2$ flux surface on a millisecond timescale.

In the simulation the transport event is emulated by increasing any transport coefficient $\mathcal{Y} \in \{A, A_i, D_i, \chi_e\}$ from their baseline value \mathcal{Y}_0 up to some maximum value \mathcal{Y}_{max} , which then exponentially decays over a timescale of $\tau_{\text{decay}} = 1 \text{ ms}$, according to

$$\mathcal{Y}(t) = \mathcal{Y}_0 + (\mathcal{Y}_{\text{max}} - \mathcal{Y}_0) \exp\left(-\frac{t - t_{\text{relax}}}{\tau_{\text{decay}}}\right) \Theta(t - t_{\text{relax}}), \quad (2.6)$$

where Θ denotes the Heaviside function. In particular, this concerns the hyperdiffusivity A in equation (2.2), the ion particle advection and diffusion coefficients A_i and D_i in equation (2.3), and the electron heat diffusivity χ_e in the energy balance equation (2.5). By selecting $A_{\text{max}} = 5 \times 10^{-7} \text{ Wb}^2\text{m/s}$, we observe an increase in the plasma current during the I_p -spike similar to the experiment ($\Delta I_p \sim 20 \text{ kA}$ for the cases studied

here). The maximum value of the other transport coefficients are set to $A_{i,\max} = -100 \text{ m/s}$, $D_{i,\max} = 100 \text{ m}^2/\text{s}$, and $\chi_{e,\max} = 100 \text{ m}^2/\text{s}$. Similar values were used in ASTRA simulations of massive gas injection scenarios in AUG by Linder *et al.* (2020) to reproduce the evolution of line-integrated electron densities from experiment.

2.3. Fragment sampling

The generation of the fragment plume is performed in two steps: a rejection sampling of fragment sizes, utilising an analytical distribution function $f(d)$ for the characteristic fragment diameter d following the pellet break-up; and then assigning velocities \mathbf{v} to the individual fragments. This results in a set of tuples $\{(d_k, \mathbf{v}_k)\}$, with $k = 1$ to the total number of fragments N_{frag} .

The fragment size probability distribution stems from a statistics-based model for the shattering of brittle materials, initially derived in the context of exploding munitions by Mott & Linfoot (1943), and then more recently by Parks (2016) in the context of shattered cryogenic pellets. This has subsequently been correlated with relevant injection parameters to experimentally measured fragment distributions (Gebhart *et al.* 2020*a,b*), which is used in this paper. For a cylindrical pellet of diameter D and length L injected with an impact velocity $v_{\perp} = v_{\text{inj}} \sin \theta_s$ (component of the injection velocity v_{inj} normal to the shatter plane at an angle θ_s), this fragmentation model yields the characteristic size distribution

$$f(d) = \alpha d K_0(\beta d). \quad (2.7)$$

Here, $\alpha = X_{\text{R}}/D$, $\beta = X_{\text{R}}/LC$, and $X_{\text{R}} = v_{\perp}^2/v_{\text{thres}}^2$, the latter of which is the ratio of the impact energy and the threshold energy required to initiate fracture in the pellet. K_0 is the modified Bessel function of the second kind accounting for the energy propagation through the pellet. The material parameters C and v_{thres} depend on the neon-deuterium content ratio f_{Ne} of the pellet, both of which are obtained from Gebhart *et al.* (2020*b*). Fragments are sampled from (2.7) in sequence until the sum of all fragment volumes exceeds the pellet volume, after which the final fragment is shrunk such that the total volume equals that of the pellet. In doing so, N_{frag} will depend on the specific random seed used during the sampling process.

The next step concerns assigning velocities to each fragment. For simplicity, the magnitude and direction are sampled independently from one another and uncorrelated to the corresponding fragment's size. The velocity magnitude v_{frag} is sampled from a normal distribution, where the mean fragment speed $\langle v_{\text{frag}} \rangle$ is assumed to be given by the average of the injection speed v_{inj} and its component parallel to the shattering surface at an angle of $\theta_s = 12.5^\circ$, i.e. $\langle v_{\text{frag}} \rangle = v_{\text{inj}}(1 + \cos \theta_s)/2$, and the spread is set to be $\Delta v_{\text{frag}}/\langle v_{\text{frag}} \rangle = 20\%$ (see Peherstorfer 2022). Finally, each fragment is assigned a direction in which it traverses through the plasma at constant speed that is sampled uniformly within a circular cone with an opening angle of 20° (Peherstorfer 2022).

2.4. Simulation setup

Each simulation presented in this paper uses initial conditions from the representative AUG discharge #40655, which is an H-mode deuterium plasma with a major radius of the magnetic axis $R_0 = 1.74 \text{ m}$, minor radius $a = 0.39 \text{ m}$ (midplane high-field side distance from R_0 to the last closed flux surface), and on-axis toroidal magnetic field $B_0 = 1.81 \text{ T}$. Reconstructed magnetic equilibrium data and relevant initial plasma profiles are taken at $t = 2.3 \text{ s}$, which is approximately the time of the SPI trigger, all of which are obtained from the Integrated Data Analysis (IDA) framework (Fischer *et al.* 2010, 2016, 2020). IDA applies Bayesian probability theory on the combined analysis of multiple diagnostics and

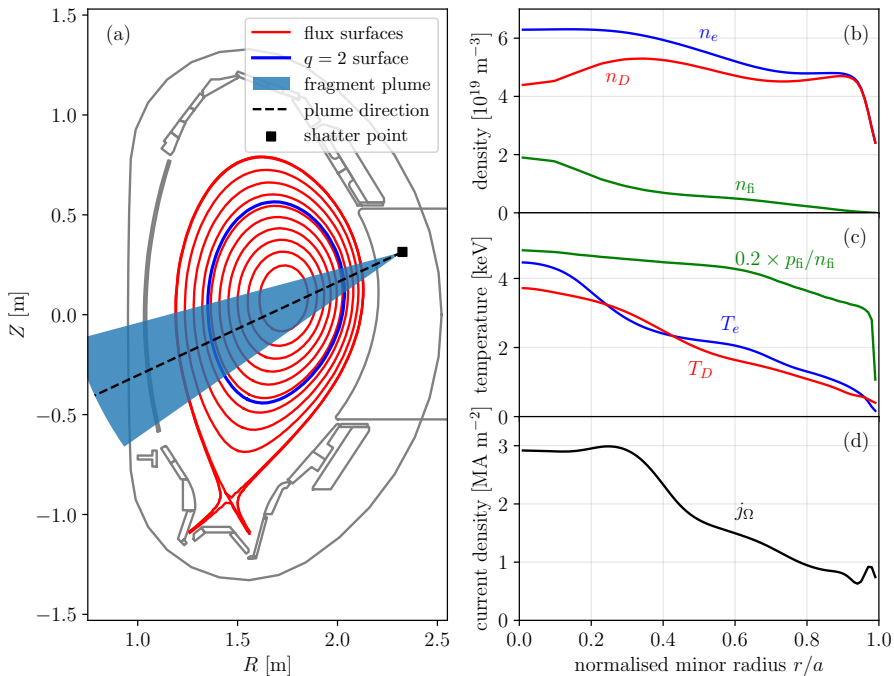


FIGURE 1. Input data based on the reference AUG discharge #40655, used in all simulations presented. An illustration (a) shows the flux surface geometry and the SPI plume, within which all fragments travel in straight lines originating from the shatter point. The particular shatter head considered in this study has a square cross section with 22 mm side lengths, and a shatter angle $\theta_s = 12.5^\circ$. Flux surfaces are indicated in red, and the $q = 2$ surface is marked in blue. The initial plasma profiles used in this work consist of (b) density and (c) temperature profiles of the bulk electrons (blue), thermal ions (red) and fast ions (green), and (d) the initial current density.

physical modelling to obtain the most cohesive profile reconstructions and uncertainty estimates.

The reconstruction of the initial electron density profile n_e is based on both deuterium cyanide laser (DCN) interferometry and Thomson scattering (TS) spectroscopy, and the electron temperature T_e is based on the latter. The initial thermal ion temperature $T_i = T_D$ is based on charge exchange recombination spectroscopy (CXRS). Furthermore, neutral beam injection (NBI) provides a non-negligible population of super-thermal fast ions, for which IDA makes estimates of the fast ion density n_{fi} and pressure p_{fi} profiles based on kinetic modelling using the RABBIT code (Weiland *et al.* 2018). With the fast ions being made up of ionised deuterium, and assuming the pre-SPI plasma is ideal, the quasi-neutrality criterion implies that the initial thermal ion density can be expressed as $n_D = n_e - n_{fi}$. The total plasma pressure $n_e T_e + n_D T_D + p_{fi}$ is then used to solve for the magnetic equilibrium in the Grad-Shafranov equation, which is done iteratively since these profiles themselves depend on the equilibrium (see Fischer *et al.* 2016).

In this model we do not resolve the momentum space distribution of any of the particle species involved. Instead, the thermal and fast ions are incorporated into a single

TABLE 1. SPI parameters used in the simulations of the considered AUG discharges, being the pellet neon fraction f_{Ne} , number of injected neon atoms N_{Ne} , pellet length L and diameter D , and pellet injection speed v_{inj} . All injections use the $\theta_s = 12.5^\circ$ shatter head with a square cross-section (GT3), as indicated in figure 1a. The final column shows the mean and standard deviation in the number of fragments generated using these parameters, based on 40 samplings of the fragment size distribution (2.7).

#	f_{Ne} [%]	N_{Ne}	L (D) [mm]	v_{inj} [m/s]	N_{frag}
40679	100	1.93×10^{22}	8.0 (9.0)	259.4	49.5 ± 15.6
40677	40	9.86×10^{21}	8.0 (9.5)	374.8	67.4 ± 23.3
40949	10	3.13×10^{21}	7.9 (11.0)	214.6	5.9 ± 2.6
40732	1.25	3.57×10^{20}	7.9 (9.7)	232.1	5.9 ± 2.7
40737	0.17	4.79×10^{19}	8.3 (8.7)	231.9	6.3 ± 2.9
40738	0	0	8.1 (10.7)	219.0	5.5 ± 2.9

Maxwellian distribution, with density $n_{\text{D}} = n_e$ and a rescaled temperature as to maintain the total plasma pressure. By doing this, it is effectively assumed that these fast ions instantaneously thermalise at the start of the simulation. It is also assumed that NBI is turned off at this point in time, meaning no further fast ions are introduced.

The corresponding flux surface geometry, with the SPI plume indicated, and the relevant plasma profiles are shown in figure 1. Note that the total current density from experiment includes bootstrap current and the NBI driven current, which is here incorporated into the Ohmic current, as shown in figure 1d. This is motivated by the fact that the bootstrap current quickly becomes Ohmic as a result of the relaxation of the pressure profile during the enhanced transport event. The NBI driven current is turned off by the control system as soon as insufficient absorption is detected, and since we do not model the complex control system logic, this contribution to the total current is omitted.

The radial coordinate is discretised on a grid with $n_r = 11$ points, and for the time coordinate we use an adaptive timestep based on the assumption that the shortest timescales are those of ionisation $\tau_{\text{ionis}} \sim |\partial \log n_e / \partial t|^{-1}$. It sets the next timestep according to $\Delta t = \min(\Delta t_{\text{max}}, \alpha \tau_{\text{ionis}})$, where we set $\Delta t_{\text{max}} = 10^{-6}$ s as the maximum allowed timestep and $\alpha = 10^{-3}$. With this setup, depending on the pellet neon content, the typical wall-clock time for the simulations considered here is between 5-15 minutes on a computer running on an AMD EPYC 9354 processor.

2.5. Experimental cases selected for comparison

The SPI system installed for the 2022 AUG SPI experimental campaign is highly flexible, with three different shatter heads, of which two have a square cross section at a $\theta_s = 12.5^\circ$ and 25° shatter angle, respectively, and the third has a circular cross section at $\theta_s = 25^\circ$. With two different shatter angles it is possible to isolate the normal impact velocity $v_{\perp} = v_{\text{inj}} \sin \theta_s$, which sets the fragment size distribution as given in equation (2.7), and the velocity distribution of the fragments v_{frag} . A detailed description of the SPI system is provided by Dibon *et al.* (2023); Heinrich *et al.* (2024a).

In this paper, all the considered cases are pellets injected via the square shatter head with $\theta_s = 12.5^\circ$ (GT3). With input conditions all based on the reference AUG discharge #40655, as described in section 2.4, only the injection parameters are modified between

the various discharges, mainly the fraction of neon f_{Ne} in the injected pellet. An overview of the different setups can be found in table 1. The values for the pellet length L , diameter D and injection speed v_{inj} are based on image processing analysis by Peherstorfer (2022). For each discharge we run 40 otherwise identical simulations with varying random seeds, resulting in a variation in the number of fragments sampled between the simulations. The last column in table 1 includes the average and standard deviation in the number of fragments.

3. Simulation results and experimental comparison

3.1. Pellet neon fraction scan

To gauge the effect of the role the pellet neon fraction f_{Ne} (or equivalently, the number of injected neon atoms, N_{Ne}) has in this dynamic system, we scan in the range between 100 % down to 0.0001 % in search of trends. Figure 2 shows the plasma current, electron temperature at the $q = 2$ surface, and the total radiated power, as functions of time for different values of f_{Ne} . The initial temperature drop in all cases is due to dilution cooling as the density is rapidly increased. With more neon introduced to the system, more energy is lost via radiation, leading to a more rapid drop in temperature, which in turn causes an earlier onset time for the enhanced transport event triggered. Since the conductivity scales as $\sigma \propto T_e^{3/2}$, a stronger temperature drop with an increasing amount of injected neon accelerates the current drop during the current quench.

For some cases with less than 5 % trace amounts of neon, or $N_{\text{Ne}} \approx 1.5 \times 10^{21}$, rather than moving in from the edge towards the $q = 2$ surface, the thermal collapse below 10 eV is initiated in the core region. When the fragments pass $R = R_0$ and reach the high-field side, they again deposit material on flux surfaces they already passed on the low-field side. For cases with neon fractions $f_{\text{Ne}} \lesssim 0.001$ %, or $N_{\text{Ne}} \lesssim 3 \times 10^{17}$, a thermal collapse does not occur, and the plasma therefore does not disrupt.

In the context of runaway electron generation, the maximum simulated runaway current is approximately 1 kA, occurring in the cases with majority neon admixture. This is mainly attributed to the larger runaway seed generated by the hot-tail mechanism due to the more pronounced thermal quench. However, the induced electric field following this drop in electron temperature is insufficient to produce a significant amount of runaway electrons from this seed population via the avalanche mechanism.

3.2. Plasma current evolution

Simulated plasma currents of six selected injection scenarios are compared with experimental measurements in figure 3. Each case was run 40 times using different realisations of the fragment sampling procedure. For the cases with a finite amount of injected neon, the simulations generally agree well with experiment. Note that since the magnetic field is kept static in the simulations, no runaway scrap-off is accounted for (Vallhagen *et al.* 2024b), and effects of vertical displacement events (VDEs) are not captured. These VDEs may explain the kink seen in the experimental data at about halfway down the current quench. In addition, we do not model any control system action, as the AUG discharge control system is too complex to implement in such a simulation, and a feed-forward implementation of the actions executed would lead to a departure from self-consistent modeling of the plasma evolution..

The last column in table 1 displays the average number and standard deviation of fragments sampled for the six injection scenarios. The fragment size distribution (2.7) has a small dependence on the neon fraction, but it is mainly the impact velocity v_{\perp} (or

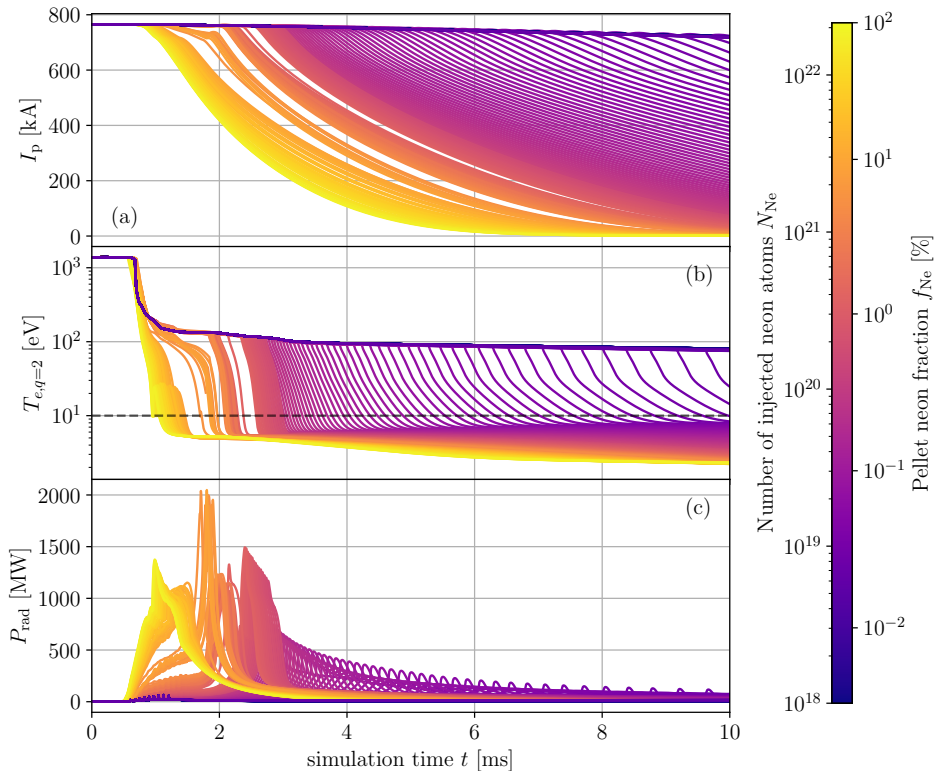


FIGURE 2. Scan in the amount of injected neon, showcasing the evolution of the (a) plasma current, (b) electron temperature at the resonant $q = 2$ surface, and the (c) total radiated power. The dashed line in (b) indicates the temperature threshold of 10 eV at which we trigger the enhanced transport event. The scan consists of 300 individual simulations, each with fragments sampled from equation (2.7) which depends on f_{Ne} .

v_{inj} , as we fix the shatter angle $\theta_s = 12.5^\circ$) that determines the size of the fragments, or equivalently the total number of fragments sampled.

In discharge #40738 no neon is introduced into the plasma, and in the simulations the radiated losses are not sufficient to initialise the enhanced transport event, meaning that the simulated plasma does not disrupt, as expected from atomic physics. In the experiment we observed a relatively long quench of the plasma current. Full-sized pure deuterium pellets injected into the AUG SPI scenario plasma typically lead to a disruption, either via an inadvertent control system action (Sieglin *et al.* 2020; Heinrich *et al.* 2024b), or as is suspected in this case, due to background impurity radiation (mainly tungsten from the first wall). The presence of background impurities provides additional loss channels through line radiation, enabling the decrease in temperature below 10 eV within the $q = 2$ flux surface, and thus triggering the enhanced transport event. However, it was also observed that 100% D_2 injections containing fewer than $N_{\text{D}_2} = 10^{22}$ deuterium molecules do not disrupt the SPI H-mode scenario (Heinrich *et al.* 2024b).

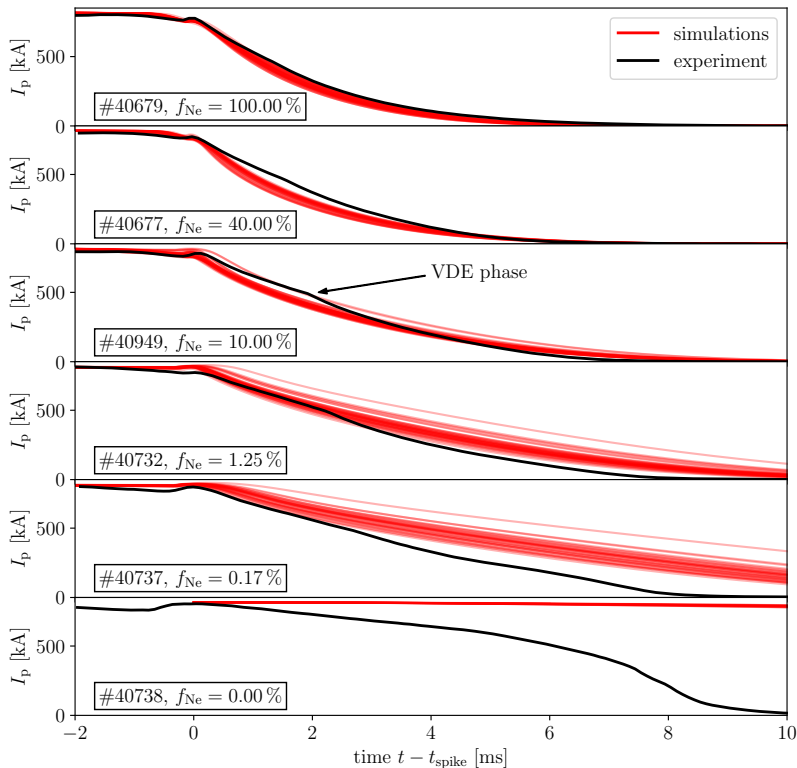


FIGURE 3. Comparison of the plasma current evolution for varying amounts of injected neon in experiment measured data (black) and simulations (red), for which each case is run 40 times using different random seeds while sampling fragments. Except for the pure deuterium injection, a good agreement with experimental plasma currents is observed during the initial current quench evolution (100 % to 80 % of I_p) prior to the onset of the VDE phase.

3.3. Radiated energy fraction

The radiated energy fraction f_{rad} shows how much of the total available plasma energy drop is lost during a disruption via radiation, as opposed to conduction. It is calculated using the formula by Lehnen *et al.* (2011) and Sheikh *et al.* (2020)

$$f_{\text{rad}} = \frac{W_{\text{rad}}}{W_{\text{th}} + W_{\text{mag}} + W_{\text{heat}} - W_{\text{c}}}, \quad (3.1)$$

where W_{rad} is the radiated energy, W_{th} and W_{mag} are respectively the initial thermal and poloidal magnetic energy, and W_{c} is the energy coupled into the surrounding conducting structure. For the simulations, the radiated energy is calculated as $W_{\text{rad}} = \int_{t_{\text{start}}}^{t_{\text{end}}} dt P_{\text{rad}}$, where the time t_{start} is when the first fragment reaches the plasma, and t_{end} is taken to be at the end of the radiation peak, when the derivative of P_{rad} approaches zero, as was done for the experimental estimates (Heinrich *et al.* 2024b). The initial thermal energy W_{th} is the combined energy of all thermal particles, i.e. $W_{\text{th}} = 3/2(n_e T_e + \sum_i n_i T_i)$, evaluated at $t = t_{\text{start}}$. Typically in AUG experiments, the heating systems automatically turn

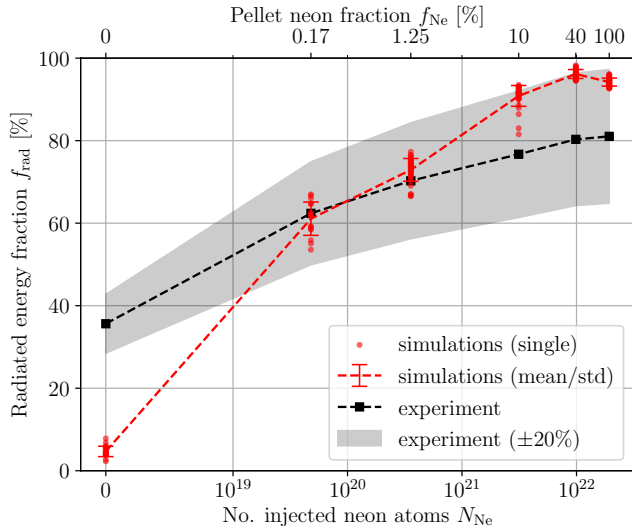


FIGURE 4. Radiated energy fraction f_{rad} from simulations (red) and experimental estimates (black) as functions of the amount of injected neon. The scatter in the simulation data comes from generating fragment samples using 40 different random seeds in otherwise identical simulations. For the experimental estimates, a relative uncertainty of 20% (gray) is assumed (Heinrich *et al.* 2024b).

off due to insufficient absorption shortly after the fragments enter the plasma, and will therefore contribute to the total energy of the system for a brief time. In the experimental evaluation of f_{rad} we correct for this by subtracting W_{heat} , which accounts for the external heating of the plasma between the arrival of fragments and shut-off of the external heating systems (Heinrich *et al.* 2024b). In the current simulation setup, we can simply assume that all heating system are effectively turned off at $t = t_{start}$, and thus we set $W_{heat} = 0$. Furthermore, the energy coupled to the surrounding structure $W_c = 0$, since we assume a perfectly conducting wall as described in section 2.1.

Figure 4 shows a comparison between the radiated energy fraction from simulations and experimental estimates, as described by Heinrich *et al.* (2024b). The calculation involves interpolating foil bolometry measurements of the radiated power in different sectors of the tokamak, and integrating it over an interval of time similarly determined as in the simulation calculations. These values have an estimated relative uncertainty of about 20%.

Another aspect – besides the plasma current – that differs between simulation and experiment for 100% D₂ deuterium injection is f_{rad} . Here it is clear that more energy is lost through radiation than seen in the simulations, which further points to the lack of background impurities in the simulation as the potential cause for this discrepancy. In these cases we observe about half of the radiation to be emitted in the TQ and VDE phases, where strong low-temperature line radiation is expected (Heinrich *et al.* 2024b). Otherwise, the simulated radiated energy fraction agrees well with experiment in both magnitude and scaling with the neon fraction.

While within the experimental uncertainty margins, f_{rad} for the highest neon fractions is close to 100% as opposed to the 80% observed in the experiments. There is yet no definite conclusion for the reason of the saturation of the experimentally observed f_{rad} around 80%. A potential cause for this may be the underestimation of conducted and coupled energy losses, both of which are difficult to self-consistently model in a 1D simulation.

4. Discussion and conclusion

We applied a one-dimensional fluid model of SPI-induced disruptions in the ASDEX Upgrade tokamak, dynamically evolving the plasma current, thermal bulk of electrons, and ion charge state densities. This numerically inexpensive model was demonstrated to yield good results when comparing to experimental data, capturing the general trend in the plasma current evolution and radiated energy fraction when varying the amount of injected neon. We also observe no significant runaway generation, as in the experiments.

A notable exception from the close agreement is the case of 100% D₂ deuterium injection, where the experiments do disrupt eventually (if $N_{D_2} \gtrsim 10^{22}$), typically due to the combined effect of background impurity radiation, reaching the density limit, vertical instability, or control system action. These aspects are not yet modelled here. In particular, the discrepancy between the simulated radiated energy fraction and the experimental estimates is primarily attributed to the absence of background impurities in the simulations. These impurities would enhance radiative energy losses, reducing the temperature sufficiently to trigger the observed enhanced transport event. Moreover, considering the plasmoid drift could lead to a higher assimilation of the injected deuterium (Vallhagen *et al.* 2023), which may also account for the observed discrepancies. The inclusion of tungsten as a background impurity in the plasma as well as the material deposition shift due to plasmoid drifts is proposed for future investigations.

A probabilistic method for generating individual fragment sizes and velocities is presented, the former of which is based on fragmentation model first proposed by Parks (2016) and modified by Gebhart *et al.* (2020*a,b*). With the present setup based on Parks, statistical variations in this sampling procedure provide an uncertainty quantification and are shown to only have a notable impact on the disruption dynamics for trace amounts of injected neon. The same is also observed experimentally.

A potential cause for discrepancies between simulation and experiment is that sampling from the Parks fragment size distribution has been shown by Peherstorfer (2022) to differ from the experimentally measured fragment size distributions at AUG. The Peherstorfer analysis was, however, limited to 4 mm diameter pellets with typically low neon content, most of which do not cause disruptions at AUG, and thus are not suitable for experimental validation of disruption simulations. Recent peridynamic modelling by Lee *et al.* (2024) has shown a promising match between modelled and measured fragment size distributions. Furthermore, reconstructed fragment size and velocity distributions from fast camera videos using a deep learning-based algorithm (Illerhaus *et al.* 2024) have become available recently. Investigating the effect of these different fragment distributions on the disruption dynamics is planned for a future study. Comparisons to 3D MHD simulations can help to inform model parameters and joint studies are planned in the future with fast 1D scans complemented by more numerically expensive non-linear 3D MHD studies of the most relevant scenarios (Tang *et al.* 2024).

Acknowledgements

The authors are grateful to S. Jachmich, J. Artola, W. Tang and A. H. Patel for the fruitful discussions. This work has been carried out within the framework of the EUROfusion Consortium, funded by the European Union via the Euratom Research and Training Programme (Grant Agreement No 101052200 — EUROfusion). Views and opinions expressed are however those of the author(s) only and do not necessarily reflect those of the European Union, the European Commission, or the ITER Organisation. Neither the European Union nor the European Commission can be held responsible for

them. The ASDEX-Upgrade SPI project has been implemented as part of the ITER DMS Task Force programme. The SPI system and related diagnostics have received funding from the ITER Organisation under contracts IO/20/CT/43-2084, IO/20/CT/43-2115, IO/20/CT/43-2116.

REFERENCES

- BERGER, ESMÉE, PUSZTAI, ISTVÁN, NEWTON, SARAH L., HOPPE, MATHIAS, VALLHAGEN, OSKAR, FIL, ALEXANDRE & FÜLÖP, TÜNDE 2022 Runaway dynamics in reactor-scale spherical tokamak disruptions. *Journal of Plasma Physics* **88** (6), 905880611.
- BOOZER, A. H. 1986 Ohm's law for mean magnetic fields. *Journal of Plasma Physics* **35**, 133–139.
- BREIZMAN, BORIS N., ALEYNIKOV, PAVEL, HOLLMANN, ERIC M. & LEHNEN, MICHAEL 2019 Physics of runaway electrons in tokamaks. *Nuclear Fusion* **59** (8), 083001.
- DIBON, M., DE MARNE, P., PAPP, G., VINYAR, I., LUKIN, A., JACHMICH, S., KRUEZI, U., MUIR, A., ROHDE, V., LEHNEN, M., HEINRICH, P., PEHERSTORFER, T., PODYMSKII, D. & TEAM, ASDEX UPGRADE 2023 Design of the shattered pellet injection system for ASDEX Upgrade. *Review of Scientific Instruments* **94** (4), 043504.
- EKMARK, I., HOPPE, M., FÜLÖP, T., JANSSON, P., ANTONSSON, L., VALLHAGEN, O. & PUSZTAI, I. 2024 Fluid and kinetic studies of tokamak disruptions using bayesian optimization. *Journal of Plasma Physics* **90** (3), 905900306.
- FIL, A., HENDEN, L., NEWTON, S., HOPPE, M. & VALLHAGEN, O. 2024 Disruption runaway electron generation and mitigation in the spherical tokamak for energy production (STEP). *Nuclear Fusion* **64** (10), 106049.
- FISCHER, R., BOCK, A., DUNNE, M., FUCHS, J. C., GIANNONE, L., LACKNER, K., MCCARTHY, P. J., POLI, E., PREUSS, R., RAMPP, M., SCHUBERT, M., STOBER, J., SUTTROP, W., TARDINI, G. & WEILAND, M. 2016 Coupling of the flux diffusion equation with the equilibrium reconstruction at ASDEX Upgrade. *Fusion Science and Technology* **69** (2), 526–536.
- FISCHER, R., FUCHS, C. J., KURZAN, B., SUTTROP, W. & WOLFRUM, E. 2010 Integrated data analysis of profile diagnostics at ASDEX Upgrade. *Fusion Science and Technology* **58** (2), 675–684.
- FISCHER, R., GIANNONE, L., ILLERHAUS, J., MCCARTHY, P. J., MCDERMOTT, R. M. & TEAM, ASDEX UPGRADE 2020 Estimation and uncertainties of profiles and equilibria for fusion modeling codes. *Fusion Science and Technology* **76** (8), 879–893.
- GEBHART, T. E., BAYLOR, L. R. & MEITNER, S. J. 2020a Experimental pellet shatter thresholds and analysis of shatter tube ejecta for disruption mitigation cryogenic pellets. *IEEE Transactions on Plasma Science* **48** (6), 1598–1605.
- GEBHART, T. E., BAYLOR, L. R. & MEITNER, S. J. 2020b Shatter thresholds and fragment size distributions of deuterium–neon mixture cryogenic pellets for tokamak thermal mitigation. *Fusion Science and Technology* **76** (7), 831–835.
- HEINRICH, P., PAPP, G., DE MARNÉ, P., DIBON, M., JACHMICH, S., LEHNEN, M., PEHERSTORFER, T. & VINYAR, I. 2024a Recipes for pellet generation and launching in the ASDEX Upgrade SPI. *Fusion Engineering and Design* **206**, 114576.
- HEINRICH, PAUL, PAPP, GERGELY, JACHMICH, STEFAN, ARTOLA, JAVIER, BERNERT, MATTHIAS, DE MARNÉ, PASCAL, DIBON, MATHIAS, DUX, RALPH, EBERL, THOMAS, HOBIRK, JÖRG, LEHNEN, MICHAEL, PEHERSTORFER, TOBIAS, SCHWARZ, NINA, SHEIKH, UMAR, SIEGLIN, BERNHARD, SVOBODA, JAKUB, THE ASDEX UPGRADE TEAM & THE EUROFUSION TOKAMAK EXPLOITATION TEAM 2024b Radiated energy fraction of SPI-induced disruptions at ASDEX Upgrade, arXiv: 2410.00591.
- HENDER, T.C., WESLEY, J.C., BIALEK, J., BONDESON, A., BOOZER, A.H., BUTTERY, R.J., GAROFALO, A., GOODMAN, T.P., GRANETZ, R.S., GRIBOV, Y., GRUBER, O., GRYAZNEVICH, M., GIRUZZI, G., GÜNTER, S., HAYASHI, N., HELANDER, P., HEGNA, C.C., HOWELL, D.F., HUMPHREYS, D.A., HUYSMANS, G.T.A., HYATT, A.W., ISAYAMA, A., JARDIN, S.C., KAWANO, Y., KELLMAN, A., KESSEL, C., KOSLOWSKI, H.R., HAYE, R.J. LA, LAZZARO, E., LIU, Y.Q., LUKASH, V., MANICKAM, J., MEDVEDEV, S., MERTENS, V., MIRNOV, S.V., NAKAMURA, Y., NAVRATIL, G.,

- OKABAYASHI, M., OZEKI, T., PACCAGNELLA, R., PAUTASSO, G., PORCELLI, F., PUSTOVITOV, V.D., RICCARDO, V., SATO, M., SAUTER, O., SCHAFFER, M.J., SHIMADA, M., SONATO, P., STRAIT, E.J., SUGIHARA, M., TAKECHI, M., TURNBULL, A.D., WESTERHOF, E., WHYTE, D.G., YOSHINO, R., ZOHN, H., THE ITPA MHD, DISRUPTION & GROUP, MAGNETIC CONTROL TOPICAL 2007 Chapter 3: MHD stability, operational limits and disruptions. *Nuclear Fusion* **47** (6), S128.
- HESSLOW, L., EMBRÉUS, O., VALLHAGEN, O. & FÜLÖP, T. 2019a Influence of massive material injection on avalanche runaway generation during tokamak disruptions. *Nuclear Fusion* **59** (8), 084004.
- HESSLOW, L., UNNERFELT, L., VALLHAGEN, O., EMBREUS, O., HOPPE, M., PAPP, G. & FÜLÖP, T. 2019b Evaluation of the Dreicer runaway generation rate in the presence of high- z impurities using a neural network. *Journal of Plasma Physics* **85** (6), 475850601.
- HOELZL, M., HUIJSMANS, G.T.A., PAMELA, S.J.P., BÉCOULET, M., NARDON, E., ARTOLA, F.J., NKONGA, B., ATANASIU, C.V., BANDARU, V., BHOLE, A., BONFIGLIO, D., CATHEY, A., CZARNY, O., DVORNOVA, A., FEHÉR, T., FIL, A., FRANCK, E., FUTATANI, S., GRUCA, M., GUILLARD, H., HAVERKORT, J.W., HOLOD, I., HU, D., KIM, S.K., KORVING, S.Q., KOS, L., KREBS, I., KRIPNER, L., LATU, G., LIU, F., MERKEL, P., MESHCHERIAKOV, D., MITTERAUER, V., MOCHALSKYY, S., MORALES, J.A., NIES, R., NIKULSIN, N., ORAIN, F., PRATT, J., RAMASAMY, R., RAMET, P., REUX, C., SÄRKIMÄKI, K., SCHWARZ, N., VERMA, P. SINGH, SMITH, S.F., SOMMARIVA, C., STRUMBERGER, E., VAN VUGT, D.C., VERBEEK, M., WESTERHOF, E., WIESCHOLLEK, F. & ZIELINSKI, J. 2021 The JOREK non-linear extended MHD code and applications to large-scale instabilities and their control in magnetically confined fusion plasmas. *Nuclear Fusion* **61** (6), 065001.
- HOLLMANN, E. M., ALEYNIKOV, P. B., FÜLÖP, T., HUMPHREYS, D. A., IZZO, V. A., LEHNEN, M., LUKASH, V. E., PAPP, G., PAUTASSO, G., SAINT-LAURENT, F. & SNIPES, J. A. 2014 Status of research toward the ITER disruption mitigation system. *Physics of Plasmas* **22** (2), 021802, arXiv: https://pubs.aip.org/aip/pop/article-pdf/doi/10.1063/1.4901251/16137172/021802_1_online.pdf.
- HOPPE, MATHIAS, EMBREUS, OLA & FÜLÖP, TÜNDE 2021 DREAM: A fluid-kinetic framework for tokamak disruption runaway electron simulations. *Computer Physics Communications* **268**, 108098.
- HU, D., NARDON, E., HOELZL, M., WIESCHOLLEK, F., LEHNEN, M., HUIJSMANS, G.T.A., VAN VUGT, D. C., KIM, S.-H., CONTRIBUTORS, JET & TEAM, JOREK 2021 Radiation asymmetry and MHD destabilization during the thermal quench after impurity shattered pellet injection. *Nuclear Fusion* **61** (2), 026015.
- ILLERHAUS, J., TREUTTERER, W., HEINRICH, P., MIAH, M., PAPP, G., PEHERSTORFER, T., SIEGLIN, B., TOUSSAINT, U.v., ZOHN, H., JENKO, F. & THE ASDEX UPGRADE TEAM 2024 Status of the deep learning-based shattered pellet injection shard tracking at ASDEX Upgrade. *Journal of Fusion Energy* **43** (14).
- IZZO, V.A., PUSZTAI, I., SÄRKIMÄKI, K., SUNDSTRÖM, A., GARNIER, D.T., WEISBERG, D., TINGUELY, R.A., PAZ-SOLDAN, C., GRANETZ, R.S. & SWEENEY, R. 2022 Runaway electron deconfinement in SPARC and DIII-D by a passive 3D coil. *Nuclear Fusion* **62** (9), 096029.
- JACHMICH, S., KRUEZI, U., LEHNEN, M., BARUZZO, M., BAYLOR, L.R., CARNEVALE, D., CRAVEN, D., EIDIETIS, N.W., FICKER, O., GEBHART, T.E., GERASIMOV, S., HERFINDAL, J.L., HOLLMANN, E., HUBER, A., LOMAS, P., LOVELL, J., MANZANARES, A., MASLOV, M., MLYNAR, J., PAUTASSO, G., PAZ-SOLDAN, C., PEACOCK, A., PIRON, L., PLYUSNIN, V., REINKE, M., REUX, C., RIMINI, F., SHEIKH, U., SHIRAKI, D., SILBURN, S., SWEENEY, R., WILSON, J., CARVALHO, P. & THE JET CONTRIBUTORS 2021 Shattered pellet injection experiments at JET in support of the ITER disruption mitigation system design. *Nuclear Fusion* **62** (2), 026012.
- JÄRVINEN, A.E., FÜLÖP, T., HIRVIJOKI, E., HOPPE, M., KIT, A. & ÅSTRÖM, J. 2022 Bayesian approach for validation of runaway electron simulations. *Journal of Plasma Physics* **88** (6), 905880612.
- KIM, CHARLSON C., LIU, YUEQIANG, PARKS, PAUL B., LAO, LANG L., LEHNEN, MICHAEL & LOARTE, ALBERTO 2019 Shattered pellet injection simulations with NIMROD.

- Physics of Plasmas* **26** (4), 042510, arXiv: https://pubs.aip.org/aip/pop/article-pdf/doi/10.1063/1.5088814/14020971/042510_1_online.pdf.
- KRAMIDA, A., RALCHENKO, Y., READER, J. & TEAM, NIST ASD 2020 NIST atomic spectra database (ver. 5.8).
- LEE, S.-J., MADENCI, E., NA, YONG-SU, DE MARNÉ, P., DIBON, M., HEINRICH, P., JACHMICH, S., PAPP, G. & PEHERSTORFER, T. 2024 Peridynamic modelling of cryogenic deuterium pellet fragmentation for shattered pellet injection in tokamaks. *Nuclear Fusion* **64** (10), 106023.
- LEHNEN, M., ALEYNIKOVA, K., ALEYNIKOV, P.B., CAMPBELL, D.J., DREWELow, P., EIDIETIS, N.W., GASPARYAN, YU., GRANETZ, R.S., GRIBOV, Y., HARTMANN, N., HOLLMANN, E.M., IZZO, V.A., JACHMICH, S., KIM, S.-H., KOČAN, M., KOSLOWSKI, H.R., KOVALENKO, D., KRUEZI, U., LOARTE, A., MARUYAMA, S., MATTHEWS, G.F., PARKS, P.B., PAUTASSO, G., PITTS, R.A., REUX, C., RICCARDO, V., ROCCELLA, R., SNIPES, J.A., THORNTON, A.J. & DE VRIES, P.C. 2015 Disruptions in ITER and strategies for their control and mitigation. *Journal of Nuclear Materials* **463**, 39–48.
- LEHNEN, M., ALONSO, A., ARNOUX, G., BAUMGARTEN, N., BOZHENKOV, S.A., BREZINSEK, S., BRIX, M., EICH, T., GERASIMOV, S.N., HUBER, A., JACHMICH, S., KRUEZI, U., MORGAN, P.D., PLYUSNIN, V.V., REUX, C., RICCARDO, V., SERGIENKO, G., STAMP, M.F. & CONTRIBUTORS, JET EFDA 2011 Disruption mitigation by massive gas injection in JET. *Nuclear Fusion* **51** (12), 123010.
- LIER, A., PAPP, G., LAUBER, PH. W., PUSZTAI, I., SÄRKIMÄKI, K. & EMBREUS, O. 2023 The impact of fusion-born alpha particles on runaway electron dynamics in ITER disruptions. *Nuclear Fusion* **63** (5), 056018.
- LINDER, O., FABLE, E., JENKO, F., PAPP, G., PAUTASSO, G., THE ASDEX UPGRADE TEAM & THE EUROFUSION MST1 TEAM 2020 Self-consistent modeling of runaway electron generation in massive gas injection scenarios in ASDEX Upgrade. *Nuclear Fusion* **60** (9), 096031.
- MARINI, C., HOLLMANN, E.M., TANG, S.W., HERFINDAL, J.L., SHIRAKI, D., WILCOX, R.S., DEL CASTILLO-NEGRETE, D., YANG, M., EIDIETIS, N. & HOPPE, M. 2024 Runaway electron plateau current profile reconstruction from synchrotron imaging and Ar-II line polarization angle measurements in DIII-D. *Nuclear Fusion* **64** (7), 076039.
- MOTT, N. & LINFOOT, E. 1943 A theory of fragmentation. *United Kingdom Ministry of Supply*.
- NARDON, E., HU, D., HOELZL, M., BONFIGLIO, D. & THE JOREK TEAM 2020 Fast plasma dilution in ITER with pure deuterium shattered pellet injection. *Nuclear Fusion* **60** (12), 126040.
- PARKS, PAUL 2016 Modeling dynamic fracture of cryogenic pellets. *General Atomics technical report GA* (A28352).
- PARKS, PAUL 2017 A theoretical model for the penetration of a shattered-pellet debris plume.
- PARKS, P. B. & TURNBULL, R. J. 1978 Effect of transonic flow in the ablation cloud on the lifetime of a solid hydrogen pellet in a plasma. *The Physics of Fluids* **21** (10), 1735–1741, arXiv: https://pubs.aip.org/aip/pfl/article-pdf/21/10/1735/12480997/1735_1_online.pdf.
- PEHERSTORFER, T. 2022 Fragmentation analysis of cryogenic pellets for disruption mitigation. *arXiv preprint* p. arXiv:2209.01024.
- PUSZTAI, ISTVÁN, HOPPE, MATHIAS & VALLHAGEN, OSKAR 2022 Runaway dynamics in tokamak disruptions with current relaxation. *Journal of Plasma Physics* **88** (4), 905880409.
- REDL, A., ANGIONI, C., BELLI, E., SAUTER, O., TEAM, ASDEX UPGRADE & TEAM, EUROFUSION MST1 2021 A new set of analytical formulae for the computation of the bootstrap current and the neoclassical conductivity in tokamaks. *Physics of Plasmas* **28** (2), 022502.
- REITER, D. 2020 The data file AMJUEL: Additional atomic and molecular data for EIRENE.
- SHEIKH, U.A., DAVID, P., FICKER, O., BERNERT, M., BRIDA, D., DIBON, M., DUVAL, B., FAITSCH, M., MARASCHEK, M., PAPP, G., PAUTASSO, G., SOZZI, C., THE AUG TEAM & TEAM, EUROFUSION MST1 2020 Disruption mitigation efficiency and scaling with thermal energy fraction on ASDEX Upgrade. *Nuclear Fusion* **60** (12), 126029.
- SIEGLIN, B., MARASCHEK, M., KUDLACEK, O., GUDE, A., TREUTTERER, W., KÖLBL, M.

- & LENZ, A. 2020 Rapid prototyping of advanced control schemes in ASDEX Upgrade. *Fusion Engineering and Design* **161**, 111958.
- SOVINEC, C.R., GLASSER, A.H., GIANAKON, T.A., BARNES, D.C., NEBEL, R.A., KRUGER, S.E., SCHNACK, D.D., PLIMPTON, S.J., TARDITI, A. & CHU, M.S. 2004 Nonlinear magnetohydrodynamics simulation using high-order finite elements. *Journal of Computational Physics* **195** (1), 355–386.
- SUMMERS, H.P. 2004 The ADAS user manual, version 2.6.
- SVENNINGSSON, I. 2020 Hot-tail runaway electron generation in cooling fusion plasmas. Master's thesis, Chalmers university of technology.
- TANG, W., HOELZL, M., LEHNEN, M., HU, D., ARTOLA, F. J., HALLDESTAM, P., HEINRICH, P., JACHMICH, S., NARDON, E., PAPP, G., PATEL, A., THE ASDEX UPGRADE TEAM, THE EUROFUSION TOKAMAK EXPLOITATION TEAM & THE JOREK TEAM 2024 Non-linear shattered pellet injection modelling in ASDEX Upgrade. *Nuclear Fusion paper in preparation* .
- TINGUELY, R A, PUSZTAI, I, IZZO, V A, SÄRKIMÄKI, K, FÜLÖP, T, GARNIER, D T, GRANETZ, R S, HOPPE, M, PAZ-SOLDAN, C, SUNDSTRÖM, A & SWEENEY, R 2023 On the minimum transport required to passively suppress runaway electrons in SPARC disruptions. *Plasma Physics and Controlled Fusion* **65** (3), 034002.
- VALLHAGEN, O., HANEBRING, L., ARTOLA, F.J., LEHNEN, M., NARDON, E., FÜLÖP, T., HOPPE, M., NEWTON, S.L. & PUSZTAI, I. 2024a Runaway electron dynamics in ITER disruptions with shattered pellet injections. *Nuclear Fusion* **64** (8), 086033.
- VALLHAGEN, O., HANEBRING, L., FÜLÖP, T., HOPPE, M. & PUSZTAI, I. 2024b Reduced modeling of scrape-off losses of runaway electrons during tokamak disruptions. *Submitted to J. Plasma Phys.* .
- VALLHAGEN, O., PUSZTAI, I., HELANDER, P., NEWTON, S.L. & FÜLÖP, T. 2023 Drift of ablated material after pellet injection in a tokamak. *Journal of Plasma Physics* **89**, 905890306.
- WEILAND, M., BILATO, R., DUX, R., GEIGER, B., LEBSCHY, A., FELICI, F., FISCHER, R., RITTICH, D., VAN ZEELAND, M., THE ASDEX UPGRADE TEAM & THE EUROFUSION MST1 TEAM 2018 RABBIT: Real-time simulation of the nbi fast-ion distribution. *Nuclear Fusion* **58** (8), 082032.
- WIJKAMP, T.A., HOPPE, M., DECKER, J., DUVAL, B.P., PEREK, A., SHEIKH, U., CLASSEN, I.G.J., JASPERS, R.J.E. & THE TCV TEAM 2023 Resonant interaction between runaway electrons and the toroidal magnetic field ripple in TCV. *Nuclear Fusion* **64** (1), 016021.